nature communications

Article

https://doi.org/10.1038/s41467-026-71352-9

Accelerated directional growth of seaweed-like iron oxide branches driven by localized electric fields of gold nanoparticles in liquid

Received: 25 July 2025

Accepted: 19 March 2026

Published online: 31 March 2026

Check for updates

Mingrui Zhou[1], Wen Wang[2] ✉, Jinyi Sun[1], Yuze Yu[1], Meng Nie[1], Hubiao Huang[1], Haimei Zheng[3] ✉, Tao Xu[1] ✉ & Litao Sun[1] ✉

Branched nanostructures have attracted significant attention due to their potential applications across diverse fields. Precise control over branched morphology is essential for enhancing their functionality, yet it remains a considerable challenge. In this work, in-situ liquid-cell transmission electron microscopy (LCTEM) is employed to investigate the controllable growth of seaweed-like iron oxide branches in the presence of charged gold nanoparticles (Au NPs) within an organic solution. In contrast to the conventional tip-splitting behavior observed in the absence of Au NPs, the branches exhibit directional and accelerated growth toward the Au NPs without further splitting. Finite-element analysis reveals that the local electric field between the charged Au NPs and the branches promotes reactant aggregation at the branch tips, thereby driving their directional and accelerated growth. This study provides insights into the growth mechanisms of seaweed-like nanostructures and highlights the potential of local electric fields for morphological control of branched structures.

Branched nanostructures have attracted increasing attention due to their distinctive structural feature and have found widespread applications in various fields[1–4], including catalysis, energy storage, environmental protection, and sustainable remediation, etc. The functional properties of branched structures are largely influenced by their structural characteristics[4–6] such as morphology, fractal dimension, and specific surface area. Consequently, precise control over the morphology of branched structures is essential for optimizing their performance in various applications.

Extensive efforts have been made to regulate the growth of branched structures by tuning growth parameters and applying external fields[7–12]. For example, modulation of precursor concentration can improve the control over fractal dimensions and surface areas of dendrites, thereby enhancing their effectiveness in water filtration and electrocatalytic applications[10,11]. The application of an electric field can guide the lateral growth of metal branches, representing a significant advancement towards safer battery technologies[12]. Despite these advances, the fundamental mechanisms governing branched structure growth at the nanoscale remain insufficiently understood, thereby limiting the rational design and synthesis of desired nanostructures.

The mechanisms governing branched morphology and growth dynamics have been extensively investigated through theoretical approaches. The morphological instability theory raised by Mullins and Sekerka attributes branched nanostructures growth to interfacial instabilities[13–15], whereas the microscopic solvability theory emphasizes that crystal anisotropy determines the growth rate and tip morphology[16–18]. If there is little or no anisotropy in the growth kinetics or interfacial energy, branches tend to undergo continuous tip splitting, ultimately evolving into a seaweed morphology[19]. The theoretical predictions of morphology development have been extensively

[1]SEU-FEI Nano-Pico Center, Key Laboratory of MEMS of Ministry of Education, Southeast University, Nanjing, China. [2]Henan Key Laboratory of Diamond Optoelectronic Materials and Devices, Key Laboratory of Material Physics of Ministry of Education, School of Physics, Zhengzhou University, Zhengzhou, China. [3]Materials Sciences Division, Lawrence Berkeley National Laboratory, Berkeley, CA, USA. ✉e-mail: wangw@zzu.edu.cn; hmzheng@lbl.gov; xt@seu.edu.cn; slt@seu.edu.cn

verified at the microscale by simulations and experiments[20–22]. However, it remains unclear whether theoretical predictions of morphology control can be reliably extended to the nanoscale, since certain assumptions and derivations in classical theories may not hold at this scale. A comprehensive understanding of morphology evolution at the nanoscale requires the use of advanced in-situ visualization techniques to reveal dynamic growth behaviors.

Recent advances in LCTEM enable the visualization of nanomaterial dynamics in liquid with high spatiotemporal resolution[23–28], providing an opportunity to study branched structures growth mechanisms at the nanoscale. In this study, LCTEM was employed to systematically investigate the growth dynamics of seaweed-like iron oxide nanostructures, while charged Au NPs were introduced into the reaction solution to modulate the branch formation. Observations revealed that the Au NPs guided the directional and accelerated growth of the branches, in contrast to the tip-splitting growth pattern observed in their absence. Finite-element analysis indicated that the local electric field between the charged Au NPs and the branches governs this directional and accelerated growth behavior.

Results

In-situ observation of seaweed-like nanostructure growth

In-situ LCTEM experiments were conducted by sealing the reaction solution within a silicon nitride (SiN_x) liquid cell (Fig. 1a and Methods). The reaction solution was prepared by dissolving $Fe(acac)_3$ in a mixture of oleylamine (OAm), oleic acid (OAc), and benzyl ether, followed by the addition of Au NPs. Iron oxide clusters were nucleated and grown into branched structures via OAm-promoted electron-beam

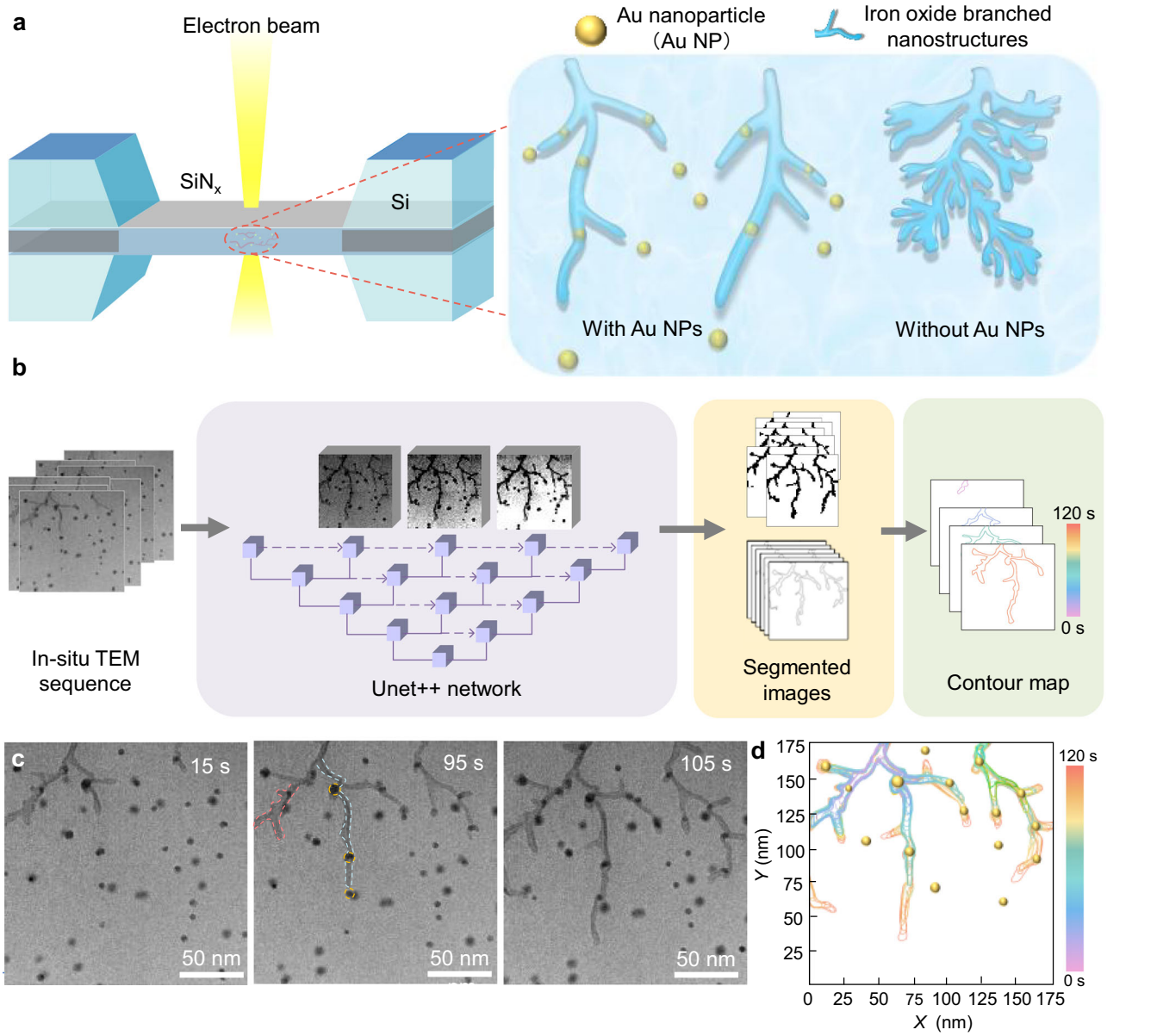

Fig. 1 | In-situ visualization of iron oxide nanostructure growth in the presence of Au NPs by LCTEM. a Schematic of the experimental setup for the dynamic observation of seaweed-like nanostructures growth. **b** Flow chat of contour extraction for TEM images based on Unet++ segmentation. **c** Sequential images from Supplementary Movie 1 and the corresponding contour map of nanostructures show the directional growth of branches towards the Au NPs. Red dashed lines outline the growth morphology of branches in the absence of nearby Au NPs. Blue dashed lines indicate the growth morphology when Au NPs are present near the branches, and Au NPs along the growth path are marked with yellow dashed lines. **d** The corresponding contour map of nanostructures in (**c**). Contours of the iron oxide nanostructures are overlaid to visualize their evolution. The color bar indicates the time sequence, with pink representing the initial stage and red representing the later stage. Intensity values are plotted on a linear scale.

https://doi.org/10.1038/s41467-026-71352-9

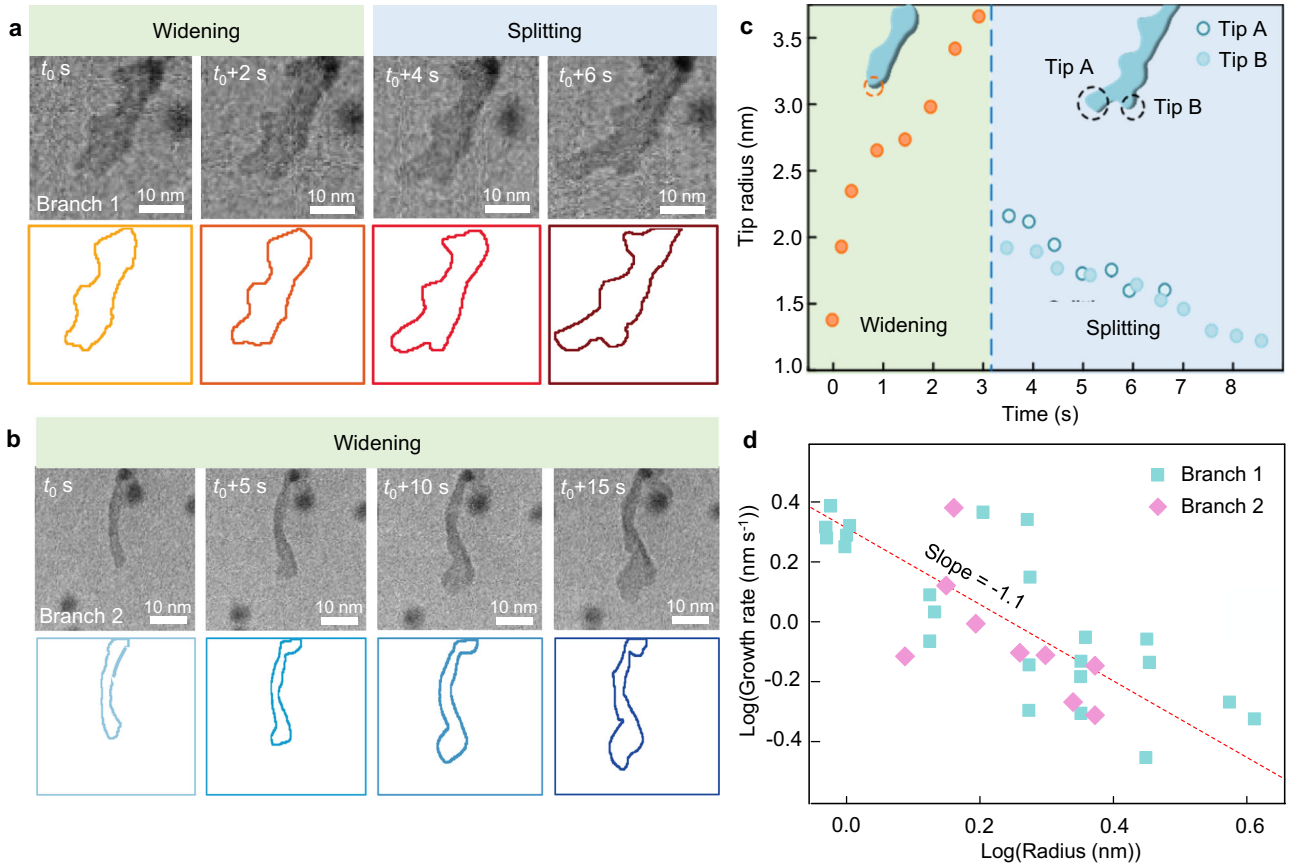

Fig. 2 | Growth dynamics of branches without Au NP guidance. a A multi-branched pattern formed as a result of tip widening and subsequent splitting. **b** A growth pattern in which the tip undergoes widening without splitting. **c** Temporal evolution of the tip radius of branch 1 during the branching process. The tip radius initially increases gradually (orange) and then decreases significantly when the tip splits into two branches (blue), forming Tip A and Tip B. **d** Logarithmic correlation between the growth rate and the curvature radius. Blue and pink represent the logarithmic relationship between the radius and growth rate of branch 1 and branch 2, respectively. The red dashed line shows the linear fitting result, with a slope of −1.1. Source data are provided as a Source Data file.

reduction, consistent with the methodology reported by Hauwiller et al.[29]. This growth pathway has been previously demonstrated to closely mimic conventional thermally activated synthesis processes of Fe_3O_4[30,31]. Post-analysis indicated that the product contains Fe_3O_4, but the presence of FeO_x cannot be excluded (Supplementary Note 3 and Supplementary Figs. 1, 2). Herein, we refer to the product as iron oxide, and subsequent analysis reveals that the specific composition makes little sense to growth mechanisms. Morphologically, the iron oxide branches observed in LCTEM do not exhibit a well-defined primary growth direction or a distinct columnar trunk[32]. As a result, the overall growth of iron oxide is described as seaweed-like growth. To enable accurate tracking and analysis of the growth dynamics, a deep learning-based method was developed to extract the contours of the nanostructure throughout the growth process (Fig. 1b and Supplementary Note 1).

Figure 1c (Supplementary Movie 1) illustrates a typical growth sequence of iron oxide seaweed nanostructures. Interestingly, when Au NPs are present near the branch tips, the branch growth exhibits a directed growth toward the Au NPs, accompanied by suppression of tip splitting and lateral widening, ultimately leading to contact between the branch and the particle (marked by the blue dashed line). In contrast, branches lacking Au NPs ahead of the growth front (highlighted by the red dashed line) undergo pronounced tip splitting and develop multi-branches, reflecting a more conventional dendrite growth mode[29] (additional comparative examples are provided in Supplementary Figs. 3–6 and Supplementary Notes 4, 5). This distinct modulation of growth behavior by Au NPs highlights their role in guiding nanostructure formation. Figure 1d shows the growth trajectories of the iron oxide nanostructures, where the color gradient from pink to red indicates the temporal evolution from the beginning to the end. It is worth noting that branched structure growth is predominantly two-dimensional (2D) on the SiN_x membrane, with only the Au NPs located on the same membrane (identified by their high contrast and well-defined contour, see Supplementary Fig. 7) exerting a significant influence on the growth behavior.

Growth kinetics of seaweed-like nanostructures

To elucidate the role of Au NPs in branch growth, a comprehensive analysis of branch growth behavior was first conducted in the absence of Au NPs. Within NP-free regions, the branches exhibit non-directional and highly branched growth. The contours of these branches throughout the growth process were extracted and are presented in Fig. 2a, b. For branch 1, the growth front initially undergoes flattening and lateral widening before splitting into two new tips, ultimately forming a small, multi-branched structure. The temporal evolution of the tip radius was quantified, revealing that the curvature radius increases during the tip-widening and subsequently decreases as splitting occurs (Fig. 2c). Pattern formation from a homogeneous liquid solution is generally governed by the competition between interfacial energy and interfacial instability. The initial broadening of the tips may be attributed to fluctuations occurring during growth. Subsequently, tip splitting occurs when the tip radius exceeds the critical threshold for morphological instability in iron oxide domains, which is ≈ 5 nm[29].

https://doi.org/10.1038/s41467-026-71352-9

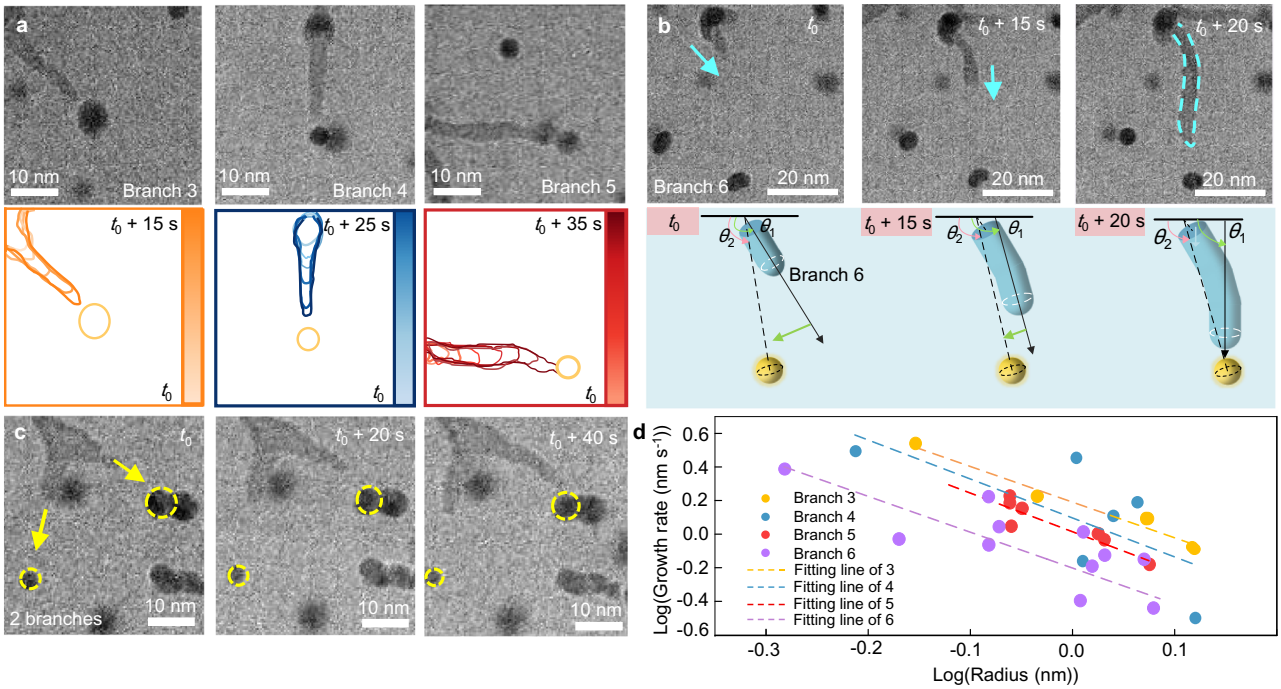

Fig. 3 | Branch growth behavior guided by Au NPs. a TEM images of directionally grown branches and corresponding time-colored contours. The growth contours of branch 3, branch 4, and branch 5 are highlighted in orange, blue, and red, respectively. The intensity values are plotted on a linear scale. **b** Changes in the orientation of the branch and the Au NP during growth (highlighted by the blue arrows and outlines). **c** Formation of two branches directed by two Au NPs (highlighted by the yellow arrows and outlines). **d** Logarithmic correlation between the growth rate and the curvature radius. Source data are provided as a Source Data file.

It is worth noting that not all growth fronts exhibit splitting behavior, as shown in Fig. 2b. This variation may be attributed to substantial precursor depletion during the growth process. As reported in refs. 19,33, seaweed-like morphology can only be achieved when the supersaturation reaches a sufficiently large level.

Furthermore, the correlation between the growth rate and tip radius in the absence of Au NPs was quantitatively analyzed. The growth rate was estimated based on the assumption of approximately unidimensional tip extension by measuring the displacement of each tip along the growth direction in each frame of the image sequence. The logarithmic correlation between growth rate and tip curvature radius displays a linear trend with a slope of ≈ −1.1 (Fig. 2d), consistent with a diffusion-controlled model for 2D dendritic growth[15]. It is obvious that a smaller tip curvature radius correlates with faster branch growth, likely due to an enhanced local concentration gradient induced by higher curvature, which facilitates more efficient material accumulation at the growth front.

In contrast, when Au NPs are present in the vicinity of the branch tip, the tip undergoes a local deflection and exhibits a growth tendency toward the direction where the NPs are located. As shown in Fig. 3a, the branches maintain a sharp forefront until making contact with Au NPs. Specifically, Fig. 3b intuitively illustrates how the NP guides the growth of the branch. Here, θ_1 denotes the angle between the horizontal axis and the branch's growth direction, while θ_2 represents the angle between the horizontal axis and the line connecting the center of the Au NP to the branch's initial growth point. It is evident that the initial growth is not oriented toward the particle, as indicated by the discrepancy between θ_1 and θ_2. The branch subsequently adjusts its trajectory to align with the position of the NP. When the NP shifts, the branch's growth direction changes accordingly. Supplementary Fig. 8 shows a strong correlation between the variations of θ_1 and θ_2. In addition, it is found that the local morphology of the nanostructures varies with the positioning of the NPs, as shown in Fig. 3c (see more information in Supplementary Movie 2, Supplementary Fig. 9 and Supplementary Note 6). When multiple Au NPs are located in front of the tips, it can give rise to a corresponding number of growing branches. These phenomenon supports the conclusion that the Au NP serves as a guide for the directional growth of branches.

In the presence of Au NPs, the logarithmic correlation between the growth rate and tip radius remains linear (Fig. 3d), with slopes ranging from −2.1 to −2.4 (−2.12 for branch 3, −2.31 for branch 4, −2.30 for branch 5, and −2.13 for branch 6). These values deviate significantly from the characteristic slope of −1, which is commonly associated with diffusion-controlled dendritic growth, suggesting a distinct growth mechanism of branches influenced by Au NPs.

To further confirm the influence of Au NPs, a comparative analysis was conducted on branches from the same primary branch under identical external conditions (e.g., liquid-layer thickness, electron-beam flux), with the sole variable being the presence or absence of NPs at the growth tip. The morphological evolution revealed a remarkable contrast. Without Au NPs, structures underwent tip-splitting, forming densely branched, seaweed-like patterns (Fig. 4a, b), a phenomenon consistently observed in control experiments where Au NPs were completely absent (Supplementary Note 5 and Supplementary Figs. 4–6). In contrast, the presence of Au NPs promoted directional growth toward the NPs and suppressed tip-splitting, resulting in sparsely branched patterns (Fig. 4a, b). To quantify these morphological differences, we calculated the fractal dimensions of the resulting structures. The absence of Au NPs yielded a fractal dimension of ≈ 1.6 (Supplementary Fig. 5), consistent with diffusion-limited aggregation (DLA) for 2D growth[34–36]. By comparison, the presence of Au NPs reduced the fractal dimension to ≈ 1.4. This quantitative analysis confirms that Au NPs alter the growth kinetics of the seaweed-like nanostructures, leading to sparser branching.

As previously noted, in the absence of Au NPs, the tip radius increases continuously until it exceeds the threshold for morphological instability, after which it rapidly decreases due to tip splitting. In contrast, branches growing toward Au NPs maintain sharp tip

https://doi.org/10.1038/s41467-026-71352-9

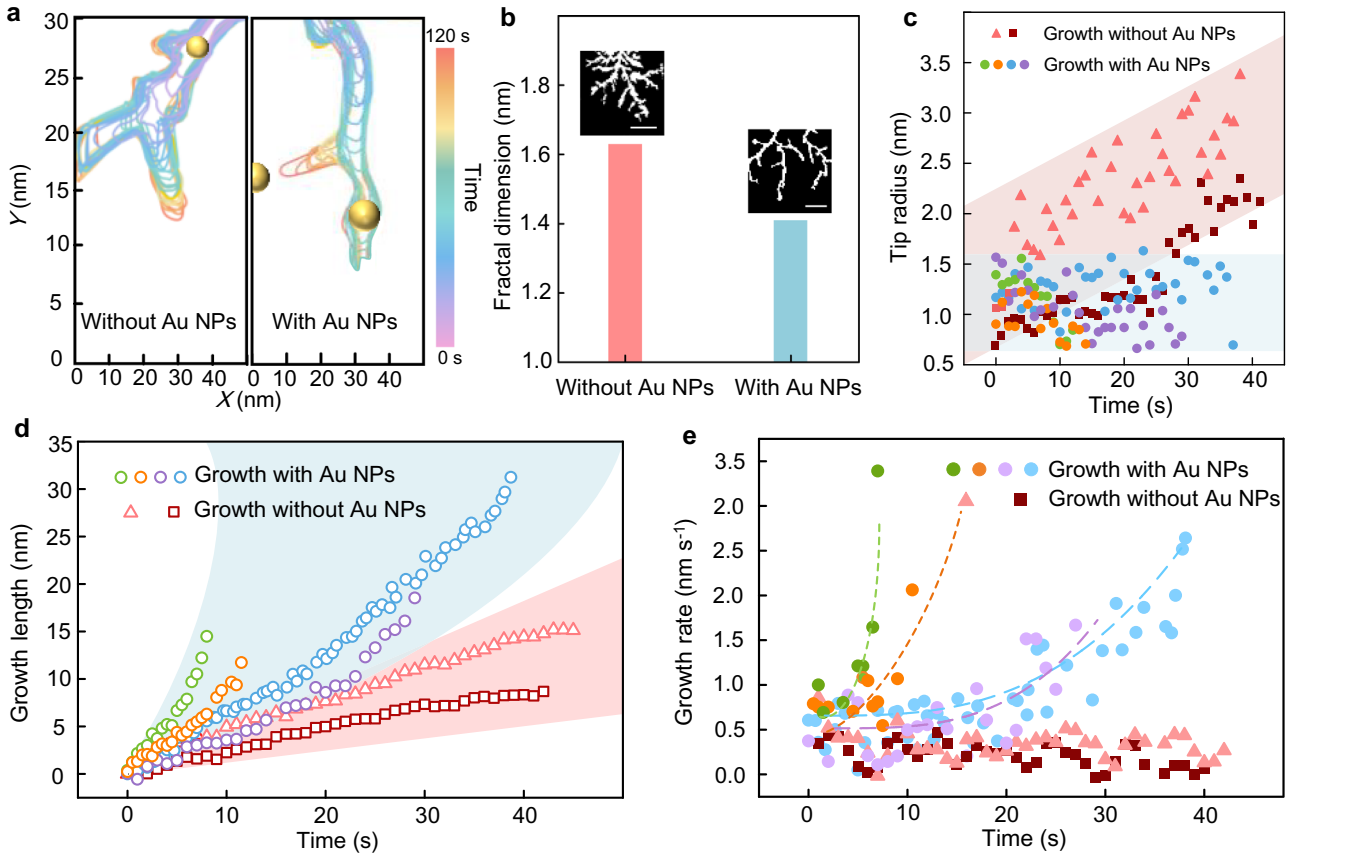

Fig. 4 | Comparison of the growth behavior of branches with and without Au NP guidance. a Time-resolved evolution of the contours of branches. Intensity values are plotted on a linear scale. **b** Fractal dimensions of branched nanostructures. The red and blue bars represent the fractal dimension values under conditions without and with Au NPs, respectively. Scale bars: 50 nm. **c** Time-dependent changes in branch tip radius. **d, e** Branch growth length (**d**) and growth rate (**e**) as a function of time. Source data are provided as a Source Data file.

geometries, with the tip radius generally remaining below 1.5 nm (Fig. 4c). This behavior suggests that Au NPs enhance interfacial stability in some way, thereby inhibiting tip widening and subsequent splitting.

In addition to morphological evolution, the growth dynamics were quantitatively assessed. Branches in the NP-free region display an approximately linear increase in length over time (Fig. 4d). As shown in Fig. 4e, the growth rate fluctuates within the range of 0–0.5 nm s^{-1} and gradually decreases over time. This temporal evolution indicates that the interfacial growth becomes limited by mass transport. As the precursor is continuously consumed, the growth rate slows down and eventually ceases. This behavior is consistent with the characteristics of diffusion-controlled growth[37].

In contrast, Au NP-guided branch growth exhibits a nonlinear increase in length, with the growth rate gradually accelerating as the growth front approaches the Au NPs. This behavior differs markedly from unguided growth and is likely driven by external forces associated with the Au NPs, which facilitate mass transport and promote directional, accelerated growth.

Discussion

Based on the comparative analysis of growth dynamics, we conclude that Au NPs play a crucial role in the directional, accelerated growth of branches. Notably, Au NPs located several tens of nanometers away can also influence the growth behavior (Fig. 1c and Supplementary Movie 1), suggesting the presence of a long-range force associated with the Au NPs that may act as the potential driving mechanism. In this study, Au NPs were synthesized using a mixture of OAm, tetralin, and chloroauric acid (see Supplementary Note 7). The synthesized Au NPs were positively charged due to surface passivation by OAm ligands, as confirmed by a zeta potential measurement of ≈ +40 mV (Supplementary Fig. 10).

For the as-grown iron oxide, OAc ligands exhibit stronger surface affinity due to their high oxophilicity, forming a passivation layer of deprotonated OAc on the surface[38–40]. As a result, the iron oxide branches are negatively charged, with the surface potential estimated to be in the range of −20 to −50 mV, depending on the tip radius and OAc concentration[41]. Consequently, a local electrostatic field is established between the positively charged Au NPs and the negatively charged iron oxide branches, which is expected to influence and modulate the growth dynamics of the branches.

To further quantitatively evaluate the effects induced by Au NPs, the finite-element method (FEM) was employed to simulate the distribution of the electric field in the vicinity of an iron oxide branch and an Au NP pair. The electric field distribution was simulated using the following equations:

$$\vec{\mathbf{E}} = -\nabla \mathbf{V} \tag{1}$$

where V is localized electric potential. The Au NP possesses a radius of 2.5 nm and a surface potential of +40 mV, whereas the iron oxide branch tip has a radius of 1.5 nm and a surface potential of −20 mV, and the separation distance between them ranges from 5 to 40 nm, consistent with experimental conditions. The distributions of the electric field at varying separation distances are presented in Supplementary Fig. 11, while Fig. 5a illustrates a representative distribution at a separation distance of 8 nm. It is evident that the electric field is directed from Au NP toward the iron oxide branch, with an enhanced

https://doi.org/10.1038/s41467-026-71352-9

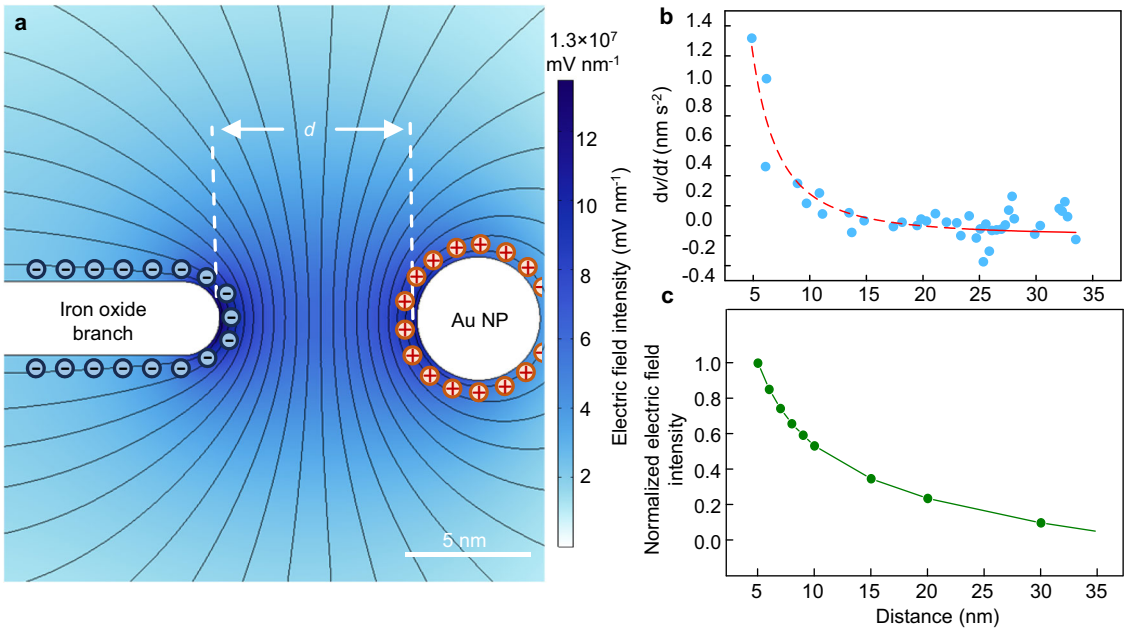

Fig. 5 | Mechanisms of directional iron oxide branch growth. a Distribution of electric field intensity around an iron oxide branch and an Au NP separated by 8 nm. Intensity values are plotted on a linear scale. **b** Variation in growth rate (dv/dt) of branch 6 as a function of the distance between the branch tip and Au NP. **c** Normalized maximum electric field intensity at the branch tip as a function of separation distance. Source data are provided as a Source Data file.

field intensity localized in the region between them. Meanwhile, the gradient of the electric field reaches its maximum along the axis connecting the Au NP and the tip of the iron oxide branch. This strong field drives the migration of positively charged reactants and intermediates toward the tip, thereby facilitating directional branch growth[42]. Although the movement of particles modifies the spatial distribution of the electric field, its overall characteristics remain consistent. As a result, the branches continue to grow toward the Au NPs, leading to the gradual bending of the branch morphology (Fig. 3b).

To quantitatively evaluate the influence of the local electric field on branch growth, variation in growth rate (dv/dt) was examined as a function of the distance (d) between the branch tip and the Au NP. As shown in Fig. 5b, when the distance exceeds 15 nm, the growth rate of branch 6 exhibits minimal variation. A significant increase in growth rate is observed as the separation distance decreases, confirming accelerated branch growth at shorter distances. Quantitative analysis reveals that the variation in growth rate is inversely proportional to the square of the separation distance, consistent with Gauss's law, thereby confirming the dominant role of the electrostatic field in governing local branch growth (Supplementary Fig. 11). In addition, the local electric field distribution in the presence of multiple NPs in solution was investigated systematically, which was consistent with the phenomena observed in our experiments (see Supplementary Note 8 and Supplementary Figs. 12–14 for more details).

The growth direction of the branch is governed by the maximum local electric field intensity at the branch tip, which is co-determined by the tip curvature and the relative spatial positioning of the NPs (Supplementary Fig. 14). As illustrated in Fig. 5c, the maximum field intensity exhibits an inverse relationship with the separation distance, indicating that the influence of the local electric field becomes increasingly pronounced as the distance decreases. This enhanced field effect leads to accelerated growth at shorter distances. However, as the distance approaches a critical threshold, the branch growth rate declines significantly (Supplementary Fig. 15). Quantitative analysis reveals this critical distance to be ≈ 4 nm in this work. This value closely corresponds to the combined molecular length of OAc and OAm ligands[43], suggesting that the observed behavior is likely due to spatial repulsion arising from steric interactions between surface ligands. When these ligands come into proximity, steric hindrance may impede the diffusion of precursor toward the growth front, thereby diminishing the local supply of reactants and inhibiting further branch elongation. Ultimately, following the displacement of the ligands, the iron oxide branches establish direct contact with the Au NP surface[44].

In summary, the dynamic growth of seaweed-like iron oxide nanostructures was investigated using in-situ LCTEM. In the absence of Au NPs, the structures exhibit tip splitting and evolve into highly branched, fractal morphologies, typical of diffusion-limited growth. In contrast, the presence of Au NPs facilitates locally directed, accelerated branch growth, resulting in sparsely branched patterns with a reduced fractal dimension. Finite-element analysis demonstrates that a local electric field forms between the positively charged Au NPs and the negatively charged iron oxide branches, facilitating reactant aggregation at the branch tips and consequently promoting directional and accelerated growth. This study provides insights into the fundamental growth mechanisms of branches influenced by local electrostatic fields and highlights the potential of employing localized external fields for morphological control. Given that the growth pathway directly dictates the structural features governing subsequent functionality, this work also provides a foundational framework for investigations into the properties of other nanostructures.

Methods

Liquid-cell experimental setup

The reaction solution was prepared by dissolving 0.5 mmol of iron acetylacetonate (99%) in a solvent mixture of OAm (90%), OAc (99%), and benzyl ether (95%) (volume ratio of 3:1:6 and 10 mL in total). A substantial quantity of Au NPs was then mixed into the liquid precursor. ≈ 50 nL of the final solution was loaded into a reservoir of the liquid cell, forming a ≈100 nm liquid layer sandwiched between two SiN_x membranes (20 nm thick each) at the observation window.

Liquid-cell fabrication

The liquid cell used in this study was fabricated based on SiN_x membranes using standard silicon microfabrication techniques (Supplementary Fig. 16). Briefly, ultrathin silicon wafers (100 μm thick, 4-inch diameter, p-type) served as substrates. A layer of SiN_x (≈ 15 nm) was

deposited on both sides via low-pressure chemical vapor deposition (LPCVD). The cell was then constructed through sequential photolithography, wet etching to define the viewing windows and reservoirs, thermal deposition of a metallic spacer to create the cavity, and final bonding.

For liquid loading, ≈ 100 nL of the reaction solution was introduced into the reservoir via a syringe equipped with a Teflon tube. The liquid was spontaneously drawn into the viewing window by capillary force, forming a thin layer confined between the two SiN_x membranes. The thickness of this liquid layer, ≈ 100 nm, was precisely defined by the height of the deposited spacer. Finally, the injection port was sealed with epoxy resin, passed a vacuum leak test, and loaded into the electron microscope for observation. During TEM imaging, the electron beam traverses this thin liquid layer sandwiched within the observation window.

TEM characterization

A JEOL 3010 TEM equipped with a Gatan Orius 833 camera was used in our experiment, operating at 300 kV with an electron beam current density of ~ 10^3–10^4 A m^{-2}.

Image processing and analysis

A deep learning approach based on the UNet++ architecture was employed to extract the contours of iron oxide nanostructures. A set of 20 images acquired during the branch growth process was manually annotated to construct the training dataset. Given the limited dataset size, various data augmentation techniques, including rotation, translation, scaling, flipping, and cropping, were applied to expand the dataset and enhance the model's performance. Image alignment across successive frames was achieved using a sliding window approach. Finally, the contours were extracted to determine the position coordinates of branch tips, which were subsequently used for quantitative analysis.

Calculation of fractal dimension

The fractal dimension was analyzed via the box-counting method with an ImageJ plugin.

Statistics and reproducibility

To ensure the reliability of our observations, all key experiments were independently repeated and carefully validated. For the tip-splitting growth behavior in the absence of Au NPs, this phenomenon was reproduced in five independent experiments. In each experiment, multiple branches were examined, and the branches consistently exhibited the two characteristic growth modes (i.e., tip-splitting or tip-widening). Representative examples are presented in the Fig. 2a, b (see Supplementary Figs. 4–6 for additional examples). For the growth with Au NPs, the experiment was repeated four times independently with similar results. In each experiment, all branches with Au NPs located near the branch tip exhibited directional growth toward the NPs, accompanied by suppression of tip-splitting. Representative examples from the total of 38 branches exhibiting this behavior are shown in Fig. 3a–c (see Supplementary Figs. 3, 9, 13 and 14 for additional examples).

Reporting summary

Further information on research design is available in the Nature Portfolio Reporting Summary linked to this article.

Data availability

The data that support the findings of this study are available from the corresponding authors upon request. Source data are provided with this paper.

References

1. Guo, K., Xu, D., Xu, L., Li, Y. & Tang, Y. Noble metal nanodendrites: growth mechanisms, synthesis strategies and applications. *Mater. Horiz.* **10**, 1234–1263 (2023).
2. Huang, W. et al. 2D PdAg alloy nanodendrites for enhanced ethanol electroxidation. *Adv. Mater.* **30**, 1706962 (2018).
3. Mariappan, V. K. et al. Antimonene dendritic nanostructures: Dual-functional material for high-performance energy storage and harvesting devices. *Nano Energy* **77**, 105248 (2020).
4. Zhang, X. et al. Structure adjustment for enhancing the water permeability and separation selectivity of the thin film composite nanofiltration membrane based on a dendritic hyperbranched polymer. *J. Membr. Sci.* **618**, 118455 (2021).
5. Liu, H. et al. Recent advances in understanding dendrite growth on alkali metal anodes. *EnergyChem* **1**, 100003 (2019).
6. Neumann-Heyme, H., Eckert, K. & Beckermann, C. General evolution equation for the specific interface area of dendrites during alloy solidification. *Acta Mater.* **140**, 87–96 (2017).
7. Vishnugopi, B. S., Hao, F., Verma, A. & Mukherjee, P. P. Double-edged effect of temperature on lithium dendrites. *ACS Appl. Mater. Interfaces* **12**, 23931–23938 (2020).
8. Wang, A., Deng, Q., Deng, L., Guan, X. & Luo, J. Eliminating tip dendrite growth by lorentz force for stable lithium metal anodes. *Adv. Funct. Mater.* **29**, 1902630 (2019).
9. Yi, Z. et al. An ultrahigh rate and stable zinc anode by facet-matching-induced dendrite regulation. *Adv. Mater.* **34**, 2203835 (2022).
10. Lu, Y. et al. Two-dimensional fractal nanocrystals templating for substantial performance enhancement of polyamide nanofiltration membrane. *Proc. Natl. Acad. Sci. Usa.* **118**, e2019891118 (2021).
11. Wang, J. et al. Twin defect derived growth of atomically thin MoS_2 dendrites. *ACS Nano* **12**, 635–643 (2018).
12. Zou, P. et al. Directing lateral growth of lithium dendrites in micro-compartmented anode arrays for safe lithium metal batteries. *Nat. Commun.* **9**, 464 (2018).
13. Mullins, W. W. & Sekerka, R. Stability of a planar interface during solidification of a dilute binary alloy. *J. Appl. Phys.* **35**, 444–451 (1964).
14. Mullins, W. W. & Sekerka, R. F. Morphological stability of a particle growing by diffusion or heat flow. *J. Appl. Phys.* **34**, 323–329 (1963).
15. Langer, J. S. Instabilities and pattern formation in crystal growth. *Rev. Mod. Phys.* **52**, 1 (1980).
16. Barbieri, A. & Langer, J. Predictions of dendritic growth rates in the linearized solvability theory. *Phys. Rev. A* **39**, 5314 (1989).
17. Haxhimali, T., Karma, A., Gonzales, F. & Rappaz, M. Orientation selection in dendritic evolution. *Nat. Mater.* **5**, 660–664 (2006).
18. Wang, L., Hoyt, J. J., Wang, N., Provatas, N. & Sinclair, C. W. Controlling solid-liquid interfacial energy anisotropy through the isotropic liquid. *Nat. Commun.* **11**, 724 (2020).
19. Chen, Y. et al. Tip-splitting instability and transition to seaweed growth during alloy solidification in anisotropically preferred growth direction. *Acta Mater.* **66**, 219–231 (2014).
20. Trivedi, R. & Kurz, W. Dendritic growth. *Int. Mater. Rev.* **39**, 49–74 (1994).
21. Yin, H. & Felicelli, S. D. Dendrite growth simulation during solidification in the LENS process. *Acta Mater.* **58**, 1455–1465 (2010).
22. Liu, H. et al. Controlling Dendrite Growth in Solid-State Electrolytes. *ACS Energy Lett.* **5**, 833–843 (2020).
23. Zhang, Q. et al. Atomic dynamics of electrified solid–liquid interfaces in liquid-cell TEM. *Nature* **630**, 643–647 (2024).
24. Ye, M. et al. Revealing dominant oxidative species in reactive oxygen species-driven rapid chemical etching. *Nano Lett.* **23**, 7319–7326 (2023).

25. Wang, W. et al. Facet-dependent cold welding of au nanorods revealed by liquid cell transmission electron microscopy. *Adv. Sci.* **12**, 2412779 (2025).
26. Ye, M. et al. Visualizing the crystallization of sodium chloride under supersaturated condition. *Nano Res* **17**, 7786–7792 (2024).
27. Wang, W. et al. Solid–liquid–gas reaction accelerated by gas molecule tunnelling-like effect. *Nat. Mater.* **21**, 859–863 (2022).
28. Wang, W. et al. Controlled oxidative etching of gold nanorods revealed through in-situ liquid cell electron microscopy. *Sci. China Mater.* **63**, 2599–2605 (2020).
29. Hauwiller, M. R. et al. Dynamics of nanoscale dendrite formation in solution growth revealed through in situ liquid cell electron microscopy. *Nano Lett.* **18**, 6427–6433 (2018).
30. Xu, Z., Shen, C., Hou, Y., Gao, H. & Sun, S. Oleylamine as both reducing agent and stabilizer in a facile synthesis of magnetite nanoparticles. *Chem. Mater.* **21**, 1778–1780 (2009).
31. Liang, W. I. et al. In situ study of spinel ferrite nanocrystal growth using liquid cell transmission electron microscopy. *Chem. Mater.* **27**, 8146–8152 (2015).
32. Utter, B., Ragnarsson, R. & Bodenschatz, E. Alternating tip splitting in directional solidification. *Phys. Rev. Lett.* **86**, 4604–4607 (2001).
33. You, H., Ding, C., Song, X., Ding, B. & Fang, J. In situ studies of different growth modes of silver crystals induced by the concentration field in an aqueous solution. *CrystEngComm* **13**, 4491–4495 (2011).
34. Dawar, A. & Chandra, A. Fractal forming species and hierarchical growth in polymer electrolyte composites: Raman mapping and role of seed particles. *Commun. Nonlinear Sci. Numer. Simul.* **18**, 959–972 (2013).
35. Ihle, T. & Müller-Krumbhaar, H. Diffusion-limited fractal growth morphology in thermodynamical two-phase systems. *Phys. Rev. Lett.* **70**, 3083–3086 (1993).
36. Tenti, J. M., Hernández Guiance, S. N. & Irurzun, I. M. Fractal dimension of diffusion-limited aggregation clusters grown on spherical surfaces. *Phys. Rev. E* **103**, 012138 (2021).
37. Kraus, T. & de Jonge, N. Dendritic gold nanowire growth observed in liquid with transmission electron microscopy. *Langmuir* **29**, 8427–8432 (2013).
38. Mourdikoudis, S. et al. Oleic acid/oleylamine ligand pair: a versatile combination in the synthesis of colloidal nanoparticles. *Nanoscale Horiz.* **7**, 941–1015 (2022).
39. Harris, R. A., Shumbula, P. M. & van der Walt, H. Analysis of the interaction of surfactants oleic acid and oleylamine with iron oxide nanoparticles through molecular mechanics modeling. *Langmuir* **31**, 3934–3943 (2015).
40. Sinha, S. et al. Multifunctional oleic acid functionalized iron oxide nanoparticles for antibacterial and dye degradation applications with magnetic recycling. *Mater. Adv.* **6**, 2253–2268 (2025).
41. Soares, P. I. et al. Iron oxide nanoparticles stabilized with a bilayer of oleic acid for magnetic hyperthermia and MRI applications. *Appl. Surf. Sci.* **383**, 240–247 (2016).
42. Toyos-Rodríguez, C. et al. A simple and reliable synthesis of superparamagnetic magnetite nanoparticles by thermal decomposition of Fe(acac)3. *J. Nanomater.* **2019**, 2464010 (2019).
43. El Mendili, Y. et al. Improvement of thermal stability of maghemite nanoparticles coated with oleic acid and oleylamine molecules: investigations under laser irradiation. *J. Phys. Chem. C.* **119**, 10662–10668 (2015).
44. Zhu, C. et al. In-situ liquid cell transmission electron microscopy investigation on oriented attachment of gold nanoparticles. *Nat. Commun.* **9**, 421 (2018).

Acknowledgements

This work was funded by the National Key R&D Program of China (Grant No.2022YFB4400100), the National Natural Science Foundation of China (Grant Nos.12234005, T2321002, 12574298, 12204422), the Key R&D Program of Jiangsu Province (BE2023009-4), the New Cornerstone Science Foundation through the XPLORER PRIZE, the China Postdoctoral Science Foundation (Grant No. 2023TQ0312). H.Z. acknowledges the support of U.S. Department of Energy, Office of Science, Office of Basic Energy Sciences (BES), Materials Sciences and Engineering Division under Contract No. DE-AC02-05-CH11231 within the in-situ TEM program (KC22ZH). The work at the Molecular Foundry of Lawrence Berkeley National Laboratory (LBNL) was supported by the U.S. Department of Energy under Contract No. DE-AC02-05CH11231.

Author contributions

W.W., H.Z., T.X. and L.S. supervised the project. M.Z. and T.X. performed in-situ TEM experiments; M.Z., J.S. and Y.Y performed TEM image processing; M.Z. and W.W. performed the simulations; M.N. and H.H. participated in data analysis. M.Z. and W.W. co-wrote the manuscript with all the authors contributing to the discussion.

Competing interests

The authors declare no competing interests.

Additional information

Supplementary information The online version contains supplementary material available at https://doi.org/10.1038/s41467-026-71352-9.

Correspondence and requests for materials should be addressed to Wen Wang, Haimei Zheng, Tao Xu or Litao Sun.

Peer review information *Nature Communications* thanks Jean-Luc Maurice, and the other, anonymous, reviewers for their contribution to the peer review of this work. A peer review file is available.